THE UNIVERSITY of EDINBURGH

Edinburgh Research Explorer

HighPressure Chemistry and the Mechanochemical Polymerization of [5]Cyclopphenylene

Citation for published version:
Qiu, L, Pena Alvarez, M, Taravillo, M, Evans, PJ, Darzi, ER, Jasti, R, Mayorga Burrezo, P, Lopez Navarrete, JT, Baonza, VG, Casado, J & Kertesz, M 2017, 'HighPressure Chemistry and the Mechanochemical Polymerization of [5]Cyclopphenylene', *Chemistry - A European Journal*.
https://doi.org/10.1002/chem.201703435

Digital Object Identifier (DOI):
10.1002/chem.201703435

Link:
Link to publication record in Edinburgh Research Explorer

Document Version:
Peer reviewed version

Published In:
Chemistry - A European Journal

General rights
Copyright for the publications made accessible via the Edinburgh Research Explorer is retained by the author(s) and / or other copyright owners and it is a condition of accessing these publications that users recognise and abide by the legal requirements associated with these rights.

Take down policy
The University of Edinburgh has made every reasonable effort to ensure that Edinburgh Research Explorer content complies with UK legislation. If you believe that the public display of this file breaches copyright please contact openaccess@ed.ac.uk providing details, and we will remove access to the work immediately and investigate your claim.

OPEN ACCESS

Download date: 05. May. 2023

High pressure chemistry and the mechanochemical polymerization of [5]-cyclo-*p*-phenylene

Lili Qiu[1], Miriam Peña-Alvarez[2], Mercedes Taravillo[2], Paul J. Evans[3], Evan R. Darzi[3], Ramesh Jasti[3], P. Mayorga Burrezo[4], Juan T. López Navarrete[4], Valentín G. Baonza[2], Juan Casado[4], Miklos Kertesz[1]

[1]Department of Chemistry and Institute of Soft Matter, Georgetown University, 37th and O Streets, NW, Washington, D.C., 20057-1227, USA.

[2]MALTA-Consolider Team, Department of Physical Chemistry I, Chemistry Faculty, University Complutense of Madrid, 28040 Madrid, Spain.

[3]Department of Chemistry and Biochemistry and Materials Science Institute, University of Oregon, Eugene, OR, 97403-1253, USA

[4]Department of Physical Chemistry, University of Málaga, CEI Andalucía Tech, Campus de Teatinos s/n, 29071-Málaga, Spain.

Abstract

We find evidence for the surprising formation of polymeric phases under high pressure for conjugated nanohoop molecules. This paper represents one of the unique cases where the molecular-level effects of pressure in crystalline organic solids is addressed and provides a suitable general approach based on vibrational Raman spectroscopy combining experiments and computations. In particular we studied the structural and supramolecular chemistry of the cyclic conjugated nanohoop molecule, [5]cyclo-*para*-phenylene under high pressures of 0 to 10 GPa. The theoretical modeling for periodic crystals predict good agreements with Raman spectra in the molecular phase. In addition we have discovered two stable polymeric phases that arise in the simulation. The critical pressures in the simulation are too high, but the formation of polymeric phases at high pressures provides a natural explanation for the observed irreversibility of the Raman spectra upon pressure release between 6 and 7 GPa. The geometric parameters show a deformation toward quinonoid structures at high pressures accompanied by other deformations of the nanohoops. The quinonoidization of the benzene rings is linked to the systematic change of the bond length alternation as a function of pressure, providing a qualitative interpretation of the observed spectral shifts in the molecular phase.

Introduction

This paper addresses the behavior under high pressures of a cyclic para-phenylene, an member of a group of exciting novel molecules [1] with unusual cyclic conjugation. [2] Cycloparaphenylene nanohoops ([n]CPPs) consist of n phenyl units joined to each other in their *para* positions.[3, 4, 5, 6] These nanohoops can be viewed as molecular (0D) analogues of the chainlike (1D) armchair single walled carbon nanotubes (SWCNTs). In particular, [5]CPP is the highest strained member of the [n]CPP series, with a strain energy of about 119 kcal/mol[7, 8]. This highly strained unique structure provides an ideal case for understanding cylindrical π-electronic effects and any intermolecular bond formation under high pressure would be facilitated by the high strain energy.

Understanding the behaviors of the materials under extreme conditions has attracted wide

interests and attentions from geoscientists, from physicists for phase transition of metals and superconductors, and for chemists for polymorphism of the organic solids to mention only a few areas. Both experimental measurements[9, 10, 11] and theoretical models[12] are used to investigate the cross-sectional deformations of the single, double or bundled carbon nanotubes. Typical experimental tools in this area include Raman spectroscopy[10], X-ray diffraction[13] and neutron diffraction.[14] Raman spectroscopy is most widely used and provides a powerful technique to study the pressure-induced changes of the sp^2 network.[15] Previous classical molecular simulations of single carbon nanotubes show the cross sectional shape changes from almost perfect circular to flattened oval or polygonised shapes under increased pressure, and then leading to collapse and the formation of a peanut shape above at least 16 GPa[16, 17].

Feasible and accurate experimental data of the intramolecular changes (either physical or chemical) taking place at high pressures are scarce and very valuable for the steady development of mechanochemistry and related areas. X-ray diffraction can be the technique of choice for these studies however it provides a detailed atomistic intramolecular information only occasionally. We show here a combined theoretical and experimental protocol for these studies which represents one of the first examples of the theoretical simulation of the structure and spectroscopy at high pressure in crystalline organic solids, the prediction of the high pressure vibrational Raman spectra and the comparison with the experimental spectra taken as a function of pressure. The good matching of theory and experiments gives access to an unprecedented picture of the processes induced by pressure.

In this paper, we describe this protocol by using current electronic structure programs that are able to simulate high pressure solid state conditions combined with the density functional theory (DFT) approach for the elucidation of the molecular spectroscopic properties and high pressure Raman experiments. For this we selected a molecular solid with a well-known crystal structure (without interfering intercalated solvent molecules), which is prone to change upon pressure as it represents a molecular section of a carbon nanotube for which high pressure studies are well described in the literature.[16, 17] In this paper we only consider [5]CPP which does not contain in their interiors any solvent or other molecules. These empty CPPs can more easily deform and their modeling is more straightforward compared to the filled nanohoops. CPP molecules are interesting because the peripheral carbons are terminated by hydrogen atoms and they retain one π-electron per carbon which are delocalized over all carbons in their approximate sp^2 hybridized state just like in SWCNTs. In this paper we focus on the pressure dependent shape changes of [5]CPP. We have recently shown[18], based on Raman spectroscopy and DFT evidence that the structures of the [n]CPPs systematically change as a function of n, starting with a partially quinonoid structure for small n gradually becoming more aromatic as n is increased. This effect is the result of the ring strain of the nanohoop that reduces benzene aromatization for small n changing the electron localization from the benzene rings to the interring bonds within the nanohoop (quinonoid structure) strongly affecting a number of vibrational frequencies called bond length alternation (BLA) modes. The main initial question of this work has been about how the flattening and aromaticity change under pressure.

This paper provides experimental Raman spectra as a function of pressure, P, between 0 and 10 GPa together with computational modeling of the geometries and Raman spectra further establishing structure-spectrum correlations for conjugated molecules and nanohoops. The crystal packing conditions also influence the molecular shapes. For instance, [6]CPP crystals are packed in

a hexagonal structure while [5]CPP has a more complex intermolecular structure incorporating herringbone packing. Scheme 1 illustrates the cross sectional change from a circular to an oval shape.

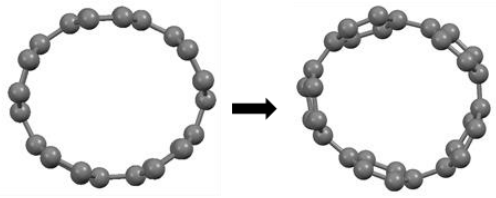

Scheme 1. Schematic deformation pathway under pressure from circular to oval showing the top view of [5]CPP. Carbons are grey, hydrogens are not shown.

In this paper, we pursuit two main objectives:

1. We will focus on the pressure dependent configurational and geometrical changes of [5]CPP which strongly affect a number of vibrational modes called bond length alternation (BLA) modes. The main initial question of this work is to explore how compression changes the cyclic configuration of [5]CPP as well as studying any possibility of pressure induce quinonoidization. For this purpose, we provide experimental Raman spectra as a function of pressure, P, between 0 and 10 GPa together with computational modeling of the geometries and Raman spectra.
2. Moreover, during simulations at high pressures above 10-11 GPa we observed a bifurcation of the total energy surface with the appearance of two low energy polymeric phases. This expanded the scope of the work to include the characterization of these polymeric phases in addition to the molecular phase allowing us to provide an interpretation of the observed irreversibility of the Raman spectra upon pressure release once the pressure reached a critical value in the experiments.

Methods

Parameters for molecular shapes: The geometries of the CPP molecules under high pressure are characterized by the changes in the local geometrical parameters shown in Figure 1a, as well as global parameters in Figure 1b that indicate the overall shape and its changes. We define three important geometric parameters to indicate the deformation of the molecules in the unit cell in the molecular phase. The first is BLA which provides a qualitative measure of the degree of the aromatic to quinonoid transformation. The second is the average torsion between adjacent phenyls. The BLA is quantitatively characterized[19] by using the following formula (**1**) and the definitions in Figure 1, where the interring torsion is also defined. When the interring bond (r) is long, and r_1 and r_2 are close in value, the structure is aromatic with BLA>0. When r is short, and $r_1 > r_2$ then BLA<0 and the structure is quinonoid. Typically, $r_1 \approx r'_1$.

$$BLA = r + r_2 - r_1 - r'_1 \qquad (1)$$

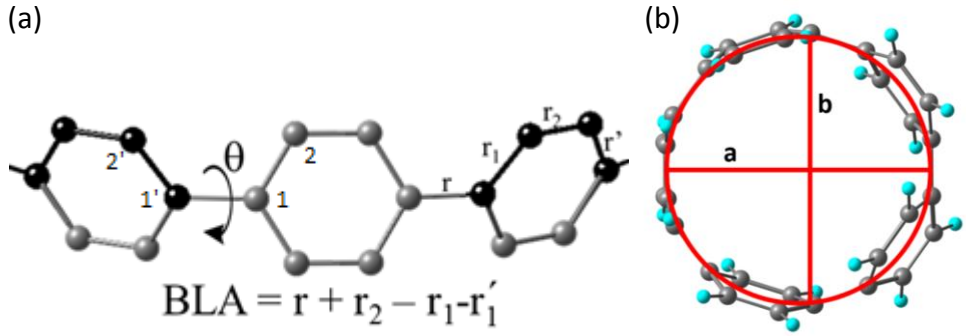

Figure 1. Geometric parameters: (a) BLA and torsional angle (θ) between two neighboring benzene units; and the CC bond distances (r, r_1, r_1' and r_2). (b) Long and short axis of [5]CPP. Carbons are grey, hydrogens are blue.

The third deformation parameter is the flattening factor f(P) showing the deformation from the approximately circular initial (P=0) shape, assuming an overall ellipsoid shape using the following formula:

$$f(P) = a(P)/b(P)\text{-}1, \qquad (\mathbf{2})$$

where *a* and *b* are the long and short axis. We obtained *a* and *b* by measuring the shortest and longest carbon-carbon distances across the molecule. Since the molecules are not perfectly circular even at P=0, the f(P)-f(0) difference is used as an approximate descriptor for the shape change under pressure.

Experimental: [5] CPP was provided by Jasti et al. and synthesized by using multinuclear arylplatinum complexes.[5] Raman measurements were carried out with a Bruker Senterra dispersive Raman spectrometer with 785 nm as excitation wavelength and spectral resolution of 3 cm^{-1} under an inert atmosphere. Pressure studies were conducted in a sapphire anvil cell (SAC). Our anvils have a diameter culet of 400 μm with which pressures up to 12 GPa can be controllably achieved. Non pressure transmitting medium was used and diamond chips were used as pressure calibrants by monitoring the 1330 cm^{-1} Raman band[20]. The frequency region associated with the calibrants bands are indicated in the experimental spectra with a gray background. The high pressure cell was loaded in a glove box under nitrogen atmosphere. Second derivative analysis of the spectra combined with Lorentzian curve fittings were used for the Raman spectra.[21]

Computational modeling: Our crystal modeling is based on the Quantum Espresso (QE) package that includes pressure as an explicit input parameter. We used PBE[22] as the density functional with the Rappe-Rabe-Kaxiras-Joannopoulos ultrasoft pseudopotential[23, 24] and a plane wave basis set with a 47 Ry cutoff. For each pressure between 0 and 20 GPa we performed full geometry optimization using default convergency criteria. For a few models we went up to 24 GPa. The consistency of our computed unit cell data with the Birch-Murnaghan equation is discussed in the SI section. The experimental structure of [5]CPP at P=1 atm≈0.0001013 GPa contains Z=8 molecules with Z'=1.[5] Due to the limited computational resources we reduced the number of molecules in the modeling to Z=2. We used two models to simplify the structure and capture the essential interactions. Figure 2a contains the full unit cell, and 2b shows both the PP and the HBP model.

HBP model (herringbone packing): This is a reasonable choice because in the unit cell of the experimentally observed [5]CPP the eight molecules can be divided into four pairs and each

pair is arranged in a herringbone packing.

PP model (parallel packing): A different kind of intermolecular interaction shown in Figure 2b and 2c is emphasized in this model also relying on two molecules per unit cell.

With the optimized geometries obtained at each P value we calculated the vibrational frequencies and non-resonant Raman intensities at the frozen geometries with the Gaussian 09 package.[25] We used the B3LYP/6-31G(d) model chemistry with non-resonant Raman intensities. The scaling factor of 0.95 was used for all frequencies.

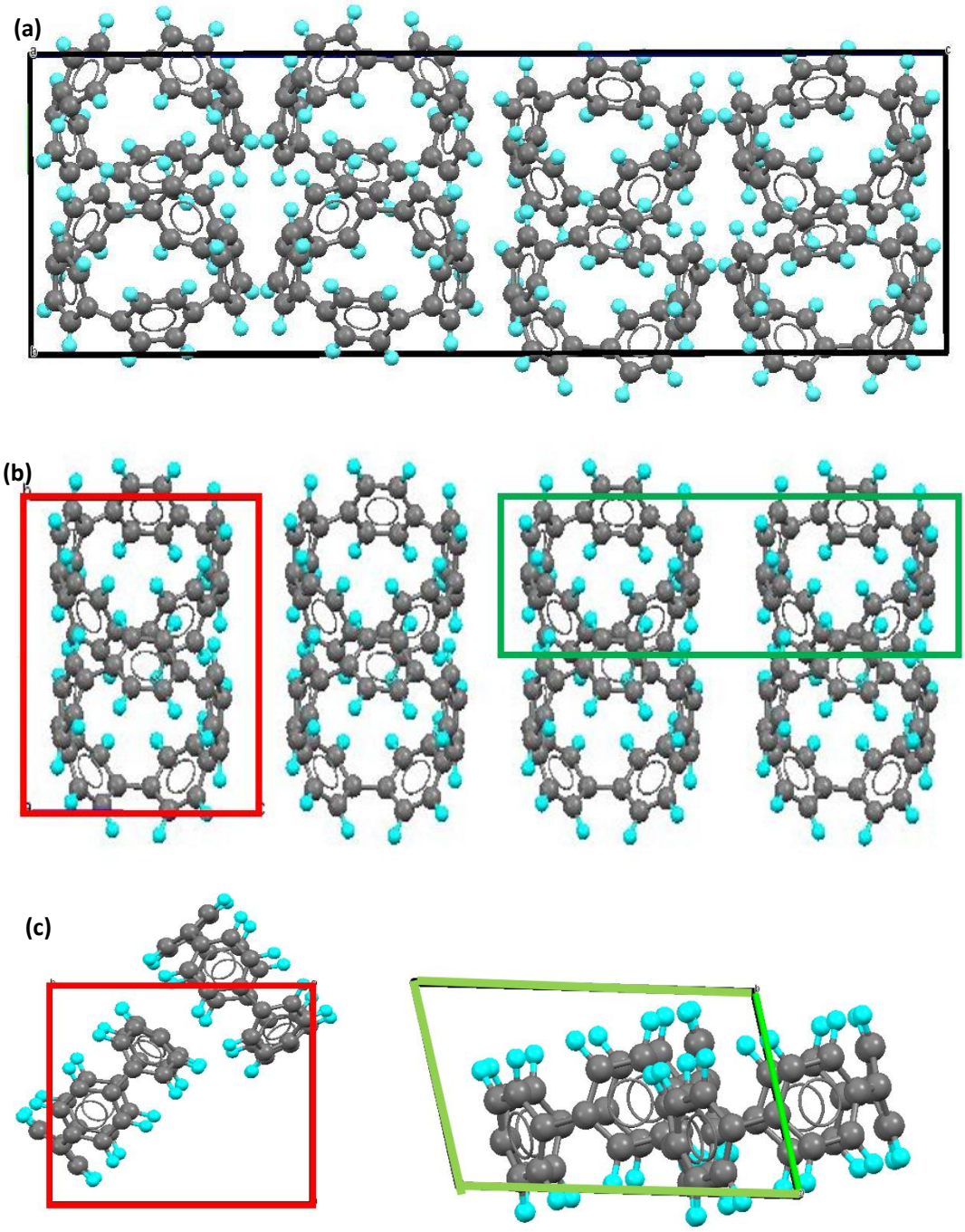

Figure 2. (a) Molecular packing in the [5]CPP crystal from X-ray diffraction[5] (Z=8). (b) Top view of two Z=2 models used in this work based on (a). (c) Side view of the unit cells used in the two unit cell models. HBP (left): **red**, PP (right): **green**.

The computed 3D structures at P=0 are summarized and compared with experiment in Figure 2 and in Table 1. The modeling at P=0 is satisfactory and forms the basis of the high pressure computations.

Table 1. The geometric parameters of the crystal unit cell of [5]CPP from X-ray diffraction and our modeling at ambient pressure.

	Experiment[5]	HBP model	PP model
Z	8	2	2
Axis a /Å	9.882	10.3499	10.2926
Axis b /Å	11.6273	11.3590	6.0782
Axis c /Å	35.5547	10.1675	18.8030
Angle α /∘	90	89.098	90
Angle β /∘	90	89.722	90
Angle γ /∘	90	90.368	75.533
Volume / $Å^3$	4064.58	1195.00	1139.04
Average Torsion /∘	12.25	3.52	2.11
Average C_{ortho}-C_{ortho} /Å	1.489	1.480	1.476

Results and discussion

Energetics, unit cell volume and a key geometrical parameter are presented in Figure 3 as a function of pressure for both HBP and PP models. As the pressure is increased the molecular crystal structures do not change significantly up to various critical pressures, which will be explained below. During the computational modeling we discovered that at high pressures major structural changes can occur and new polymeric phases are found.

We first describe the overall energetics and volumes as a function of P of all phases. Then we characterize the structures and finally turn to the Raman spectra. We will pay particular attention to the issue of reversibility as function of P.

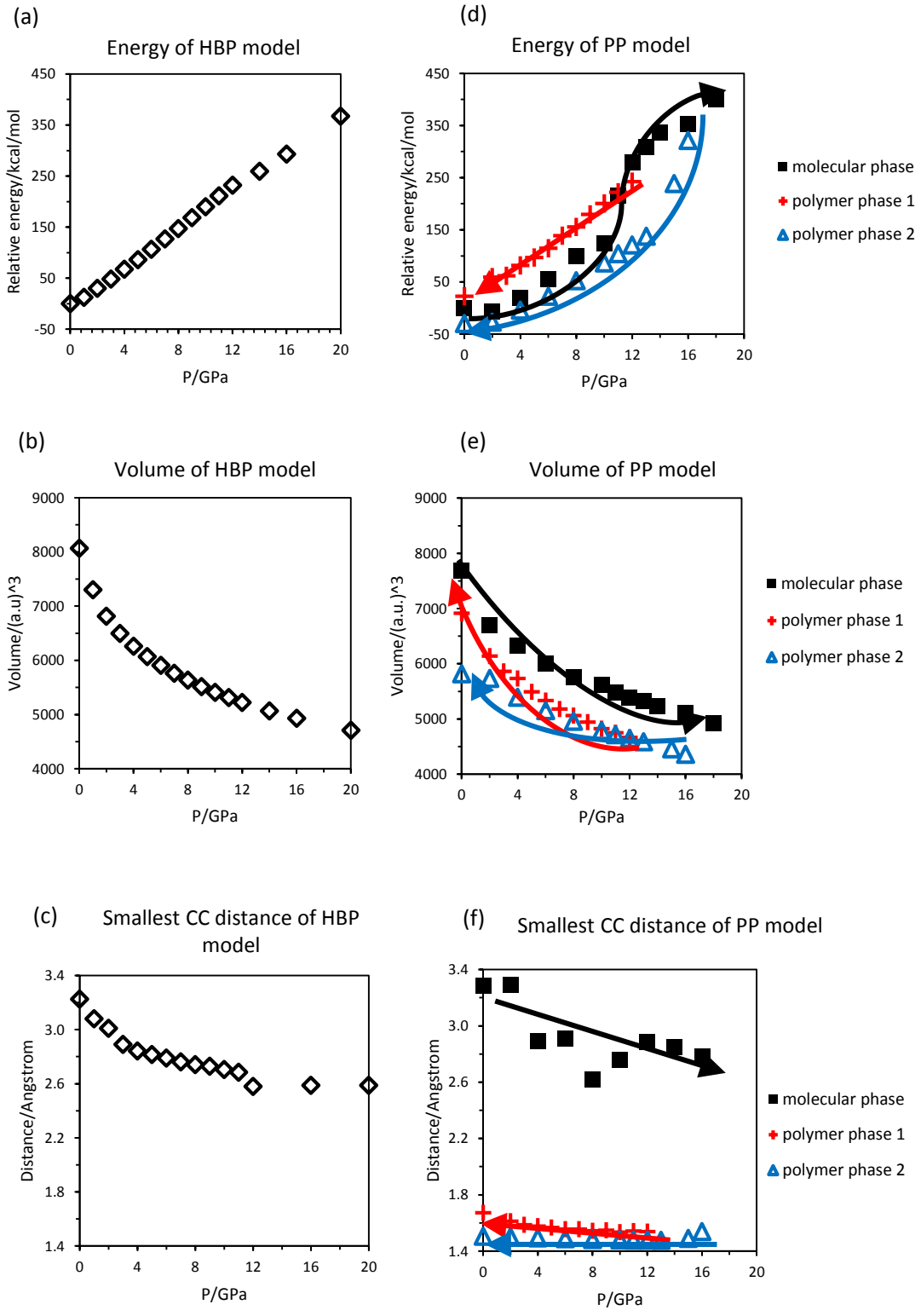

Figure 3. Pressure dependence of parameters of [5]CPP. (a) and (d): relative total energy per unit cell. (b) and (e): unit cell volume. (c) and (f): smallest inter-CPP carbon-carbon distances (see text). (a), (b), and (c) in the left column are from the HBP model and (d), (e) and (f) in the right column are from the PP model. Arrows are only provided to guide the eye and indicate the direction of pressure change. Red and blue refer to two different polymer phases, polymer-1 and polymer-2 that appear at ~11 GPa and ~16 GPa, respectively.

Within the HBP model the molecules remain unbroken and the shortest inter-CPP carbon-carbon distances remain intermolecular contacts up to the pressures investigated. Their values start out as somewhat shorter than ordinary van der Waals (vdW) contacts and decrease substantially below vdW values as expected under several GPa pressure. More details about how the molecules are deformed under pressure are discussed below. The volume change is normal and conforms to a regular Birch-Murnaghan equation as discussed in the SI section.

The PP model however, behaves very differently. The total energies of the molecular phase as the pressure is increased behave similarly to the HBP model (which has only a molecular phase) but at a critical pressure around 11 GPa the energy of the polymer-1 phase becomes lower. There is a dramatic structural change at this pressure resulting in intermolecular bond formation and reduction of the unit cell volume. A second polymer phase, polymer-2, occurs at an even higher critical pressure at about 16 GPa. Both polymers will be characterized below. If the pressure increase stops below 16 GPa, polymer-2 is not generated. Once either of these polymers are generated in the simulation, and the pressure is lowered, the prediction is that the polymer phase will remain more stable than the molecular phase. The per molecule energy at P=0 of polymer-1 is higher than that of the molecular phase by 22.7 kcal/mol, and that of polymer-2 is lower by 29.9 kcal/mol. These energy differences appear small given that they represent one new CC bonds per molecule in polymer-1 and two in polymer-2. We attribute this to the high level of strain present in the polymeric phases, as will be seen below.

We describe the polymeric phases now. Scheme 2a and 2b displays the bonding patterns of the monomer using two different valence bond (VB) structures at P=0, 2b being much higher in energy than 2a. The radical sites develop into connecting sites at high pressures in polymer-1 shown in Scheme 2c. The structural diagram shows why in polymer-1 a new pattern of aromatic and quinonoid benzene rings appears.

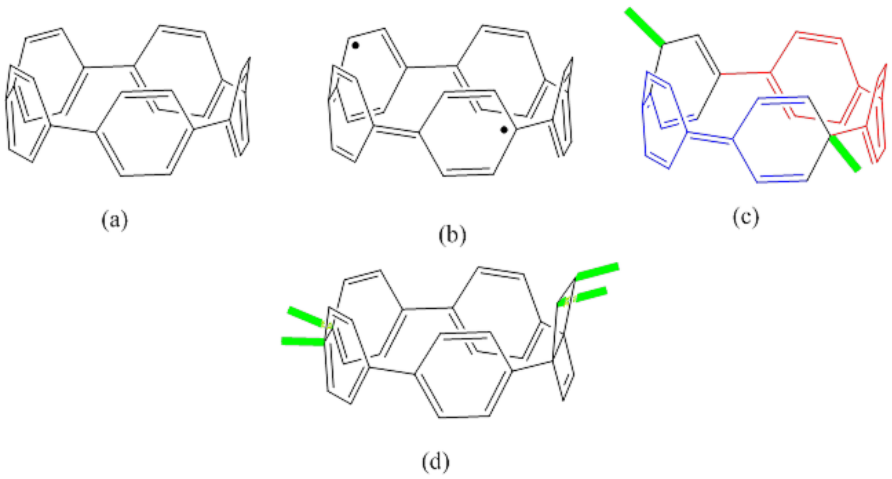

Scheme 2. Bonding in an isolated [5]CPP with two different VB patterns: (a) represents the stable covalent and (b) one of the high energy diradicaloid VB structures. (c) The bonding pattern in a repeat unit of polymer-1 closely related to the diradicaloid structure in (b). (d) Repeat unit of polymer-2. Red: aromatic benzene rings, blue: quinonoid region, green: bonds in the polymer phase connecting the [5]CPP-derived repeat units.

Scheme 3 shows both polymers at P=0 obtained from simulations after relaxing the pressure to zero from high pressure where these polymers appeared. They display two completely different

polymerization patterns. Polymer-1 has one new σ-bond per molecule connecting it in both directions. This bond disrupts the conjugation along [5]CPP creating two half nanohoops one of which retains the aromatic character of the benzene units, and the other half is converted into benzenes with strong quinonoid character as illustrated in Scheme 2c. For this reason we computed the BLA for these two segments separately and these are shown in Figure 5 as a function of pressure to be discussed subsequently.

Polymer-2 has two new σ-bonds per molecule. These bonds disrupt the conjugation in CPP even more than in polymer-1 constraining the delocalized π-electrons into two localized regions in a manner that is more symmetrical than in polymer-1. BLA is less important in characterizing polymer-2 because all benzene units are aromatic. It is worth noting that conjugated molecules have a variety of ways to form intermolecular σ-bonds by converting π-electrons and disrupting π-conjugation. For example, benzene's phase diagram contains various polymeric phases and a large number of stable phases have been described for benzene at the high pressure of 20 GPa.[26] [5]CPP molecules have much lower symmetry than benzene, and the loss of conjugation is facilitated by the high strain energy (119 kcal/mol[7]) to begin with resulting in a relatively lower critical pressure compared to the 20 GPa value of benzene.[27] Using the definition of "degree of saturation" for the number of four-coordinate carbon atoms per repeat unit from ref. [26] (where this definition is based on a per benzene unit basis) we find that polymer-1 is a degree-two, and polymer-2 is a degree-four system. It is interesting to note that polymer-2 at P=0 has a C_s symmetry cutting across the connecting C_4 rectangle consisting of sp^3 carbons. The symmetry disappears at high pressures, and the nanohoops show dents at positions where the neighboring polymers impinge on the ring, as illustrated in Figure S16.

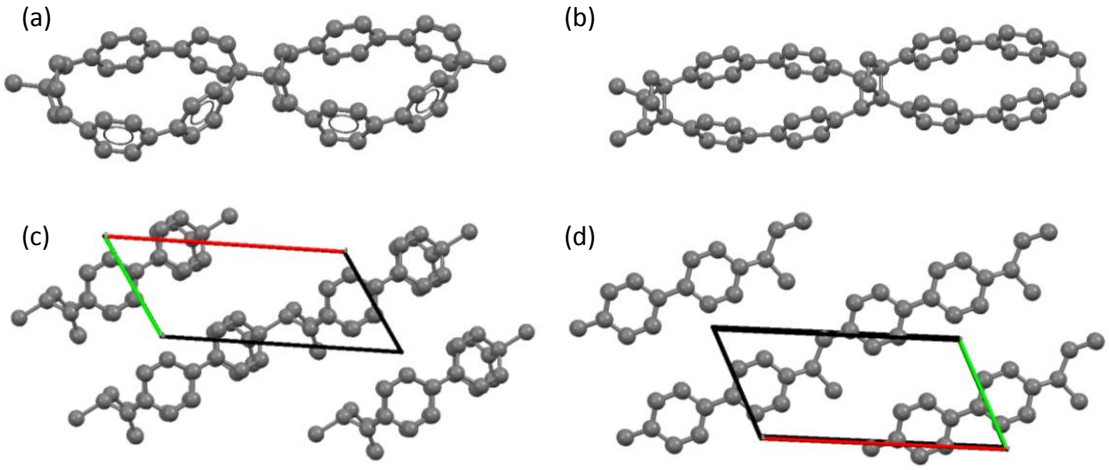

Scheme 3. Two types of polymers at P=0 GPa in the PP model. (a) Two units of polymer-1. (b) Two units of polymer-2. (c) Unit cell of the polymer-1 phase, side view. (d) Unit cell of the polymer-2 phase, side view.

Turning to the deformation of the [5]CPP nanohoops under pressure, we collected relevant data in Figures 4 and 5. Figure 4 shows the average bond distances. We use where we present structural indicators of average bond distances, BLA, torsion and flattening factor, as a function of external pressure. Since not all benzene rings within [5]CPP are equivalent, the displayed values correspond

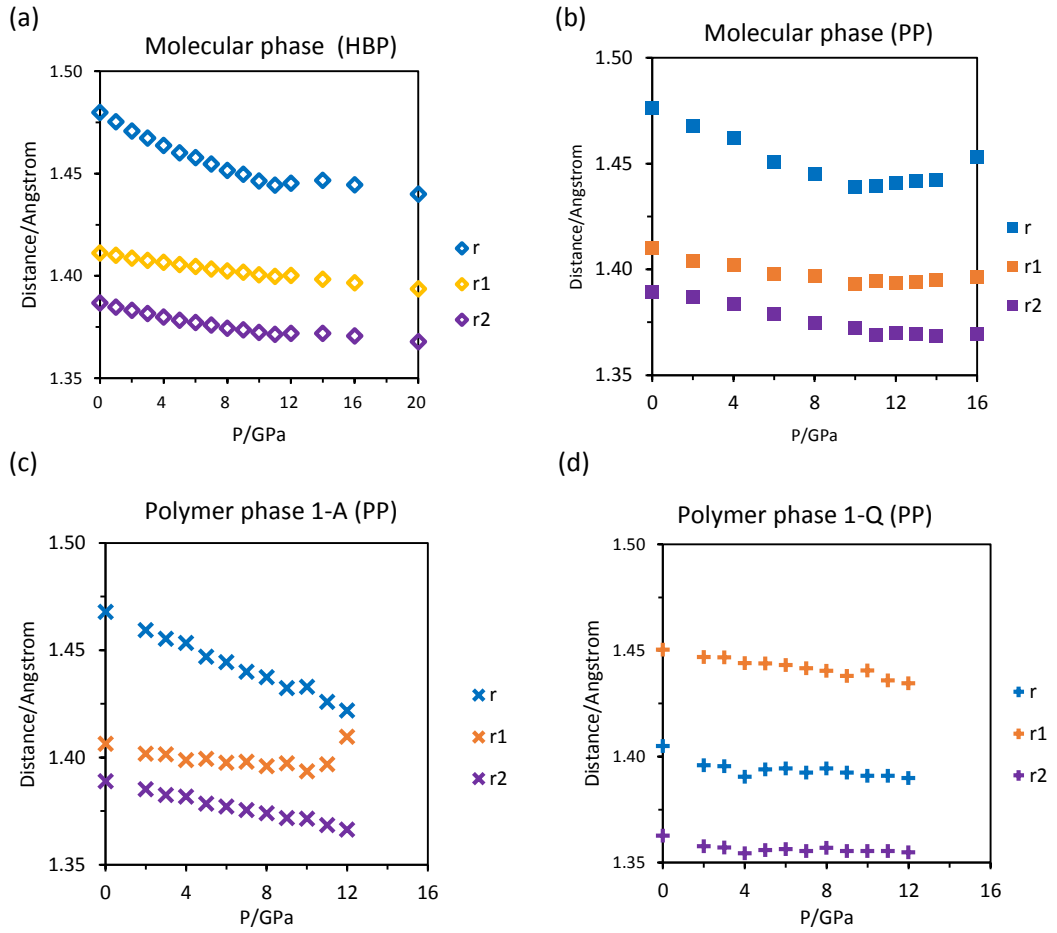

Figure 4. Geometrical parameters provided by the modeling as a function of pressure. Three types of average bond lengths are shown as defined in Figure 1. (a) and (b) refer to the molecular phase, (c) and (d) to the polymer-1 phase. Numbers in (c) refer to the aromatic parts of the nanohoops, while those in (d) refer to the quinonoid parts of the nanohoops of the polymer-1 phase.

to averages. The BLA values are computed from the r, r_1, and r_2 values as defined in Figure 1a, and they clearly reflect the aromatic vs. quinonoid nature of the nanohoops which in turn depend on a combination of factors such as bending angles (shown in Figure S15) and thus also depend on the local π-conjugation. Given the highly strained nature of the [5]CPP molecules even at ambient pressure, the molecules display cyclic conjugaton.[18]

First we discuss the molecular phase. Positive large BLA indicates a strongly aromatic structure while negative BLA is characteristic for a quinonoid structure. The computed BLA values with increasing pressure smoothly move toward smaller positive values in both models, which suggests that the deformed structure under high pressure become less aromatic than the P=0 structures. However, even at 12GPa, [5]CPP still keeps its aromatic character to some extent in the HBP model because the r values (bonds connecting the benzene rings) become shorter but do not reach typical double bond values. This trending confirms our assumption that high pressure squeezes the empty [5]CPP nanohoops toward the quinonoid direction. As we will discuss the experimental Raman spectroscopy is consistent with these trends.

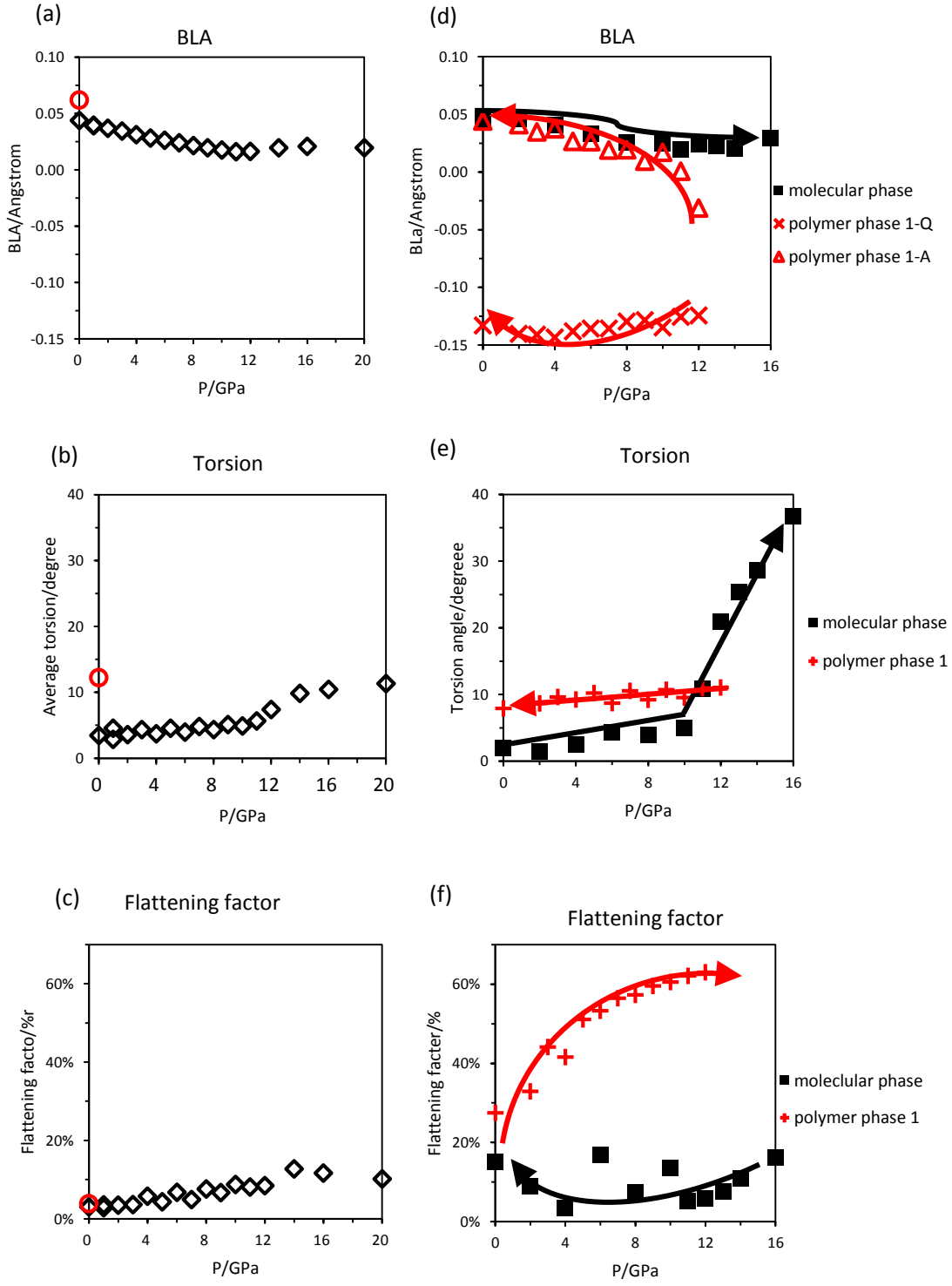

Figure 5. Geometrical parameters as a function of pressure for [5]CPP. (a) and (d) show average bond length alternations. (b) and (e) show average torsions. (c) and (f) show flattening factors. Values from the experimental XRD data are indicated by red crosses. (a), (b), and (c) in the left column are from the HBP model and (d), I, and (f) in the right column are from the PP model.

The torsions of [n]CPPs are not zero due to the steric repulsions of the hydrogens on the at the 2 – 2' positions. The torsion gradually increases upon increasing pressure for [5]CPP although the values remain small up to ~11 GPa in both models. The small torsions are in line with the development of shortened *para* carbon – carbon bonds with some double bond character toward an overall quinonoid structure under high pressure, which is also consistent with the smaller BLA values seen in Figure 5a. Taken together, BLA and average torsion provide a response to pressure that indicates a qualitatively inverse relationship. For [5]CPP the flattening factor curve indicates a large deformation toward an elliptical shape similar to that predicted for single walled carbon nanotube simulations mentioned in the introduction.[16] This deformation is more pronounced in the PP model and less in the HBP model. The computed flattening factor at P=0 is 3.1% to be compared with the experimental XRD structure which yielded 3.8% in the HBP model but significantly larger in the PP model. The increase in the flattening factor upon pressure reduces the approximate circular symmetry thereby leading to the splitting of several Raman bands. This splitting into subbands is a major general feature of the observed pressure effect in the molecular phase and is seen in both the computations and the experiments. The oscillatory disparities of some of the flattening factor values at some adjacent pressures is due to the arbitrariness in the definition of the axes of an approximately elliptically shaped nanohoop.

The geometry of polymer-1 is characterized by two segments, one being clearly aromatic and the other being quinonoid in each nanohoop. Given the low symmetry and diversity of the local environments, i.e. the fact that in polymer-1 all five benzene derived rings are different, one expects a much more complex Raman spectrum compared to the molecular phase. (See Scheme 2c.) The resulting Raman spectrum should contain new lines and broadened lines compared to the molecular phase. The geometry of polymer-2 is very different from polymer-1. It has C_s symmetry, and four of the benzene rings out of five remain largely unaffected and aromatic, while the fifth is highly distorted almost beyond recognition, as shown in Figures 4b and S13.

Next we discuss the experimental Raman observations to be followed by the computed Raman spectra. Figure 6 shows the main Raman bands and their assignments at P=0 are given in Table 2. To validate our approach, selected strong experimental Raman frequencies at P=0 are compared in the Table 2 with three theoretical results using B3LYP/6-31G(d). The first refers to the isolated molecule with the geometry of the optimized single molecule. The next two refer to the molecule whose geometry has been optimized in the crystal phase by using Quantum Espresso within the HBP and PP models, respectively. The symmetry labels are approximate and refer to the idealized D_{5h} symmetry.

Table 2. Experimental and theoretical wavenumbers (in cm^{-1}) of the main peaks for [5]CPP.

Sym. based on D_{5h}	Vibrational description[a]	Experiment at ambient pressure	Theor. Crystal HBP model	Theor. Crystal PP model	Theor. Isolated molecular
A_1'	RBM	257	260	258	249
E_2'	p-RBM	266	269	277	281
E_2'	Phenyl twisting	406	425	425	421
A_2'	Phenyl rocking	420	445	453	471
E_2'	p-RBM	502	491	486	488
E_2'	RFM	505	497	498	496
E_2'	Phenyl rocking and stretch	719	696	697	696
A_1'	β(CC)+ $\beta_{antisym}$(phenyl) + RFM (for CPPs) + β(C-H)	790	785	771	774
A_1'	β(CC)+ $\beta_{antisym}$(phenyl) + RFM (for CPPs) + β(C-H)	802	802	788	786
E_2'	β(CC)+ $\beta_{antisym}$(phenyl) + RFM (for CPPs) + β(C-H)	832	816	837	811
E_2'	β(phenyl)+ ν(C-C)+ ω(CH)	1188	1184	1193	1162
A_1'	β(C-H) + $\nu(C\text{-}C)_{interring}$	1190	1185	1198	1164
E_2'	β(phenyl) + $\nu(C\text{-}C)_{interring}$ + β(C-H)	1240	1241	1242	1213
E_2'	β(phenyl) + $\nu(C\text{-}C)_{interring}$ +b(C-H)	1244	1243	1243	1214
A_1'	ν(C-C) + ω(CH) + β(phenyl)	1254	1253	1255	1215
E_2'	G_{io}: $\nu(C_{ipso}\text{-}C_{ortho})$	1504	1494	1499	1476
A_1'	G_{A1g}: $\nu(C\text{-}C)_{transversal}$	1555	1552	1552	1537
E_2'	G_{E2g}: $\nu(C\text{-}C)_{trans}$ + $\nu(C\text{-}C)_{long}$	1572	1577	1576	1561

[a]Vibrational modes have been assigned in ref. [13]. RBM Radial breathing mode, p-RBM: pseudo RBM mode. RFM: radial flexural mode or C_{ipso}-C_{ipso} bond vibration with motion outward relative to the center of the macrocycle and the C_{ortho}-C_{ortho} bond motion inward; β(C-C): C-C bond bending mode; $\beta_{antisym}$(pheny): antisymmetric phenyl breathing mode, C_{ortho}-C_{ortho} with motion inward relative to the benzene center, C_{ipso} outward. β(phenyl): symmetric phenyl breathing mode; ω(CH): C-H wagging mode; $\nu(C\text{-}C)_{interring}$: C-C inter-benzene-ring stretching mode; β(C-H): C-H bending mode; $\nu(C_{ipso}\text{-}C_{ortho})$: C_{ipso}-C_{ortho} inter-benzene-ring stretching mode; $\nu(C\text{-}C)_{transversal}$: C-C stretching mode along the transversal direction of the macrocycle; $\nu(C\text{-}C)_{long}$: C-C stretching mode along the longitudinal direction of the benzene ring.

The agreement between the experiment and the computations at P=0 is very good and as expected the predicted vibrational bands from the optimized crystal structures give better agreements than those computations based on isolated molecules. This is remarkable since this comparison highlights how normal modes and the observable vibrational frequencies are affected by and give account for the molecular environment, a critical aspect for undertaking solid state

studies and the particular effect of crystal congestion among molecules with highly polarizable π-electronic structures such as highly the strained [5]CPP. Therefore it is reasonable to use the solid state geometry optimization results to predict Raman spectra at high pressures. In the following section, the discussion of the Raman spectrum will be divided into three regions (220-900 cm^{-1}, 1100-1350 cm^{-1} and 1500-1650 cm^{-1}).

The following discussion concentrates on the pressure dependency of the main peaks in the Raman spectrum of [5]CPP as the pressure is increased in the molecular phase. The discussion is based on Figures 6, S4-S10 and especially Figure 7 which shows the pressure dependence of the frequencies of the main bands within the molecular phase.

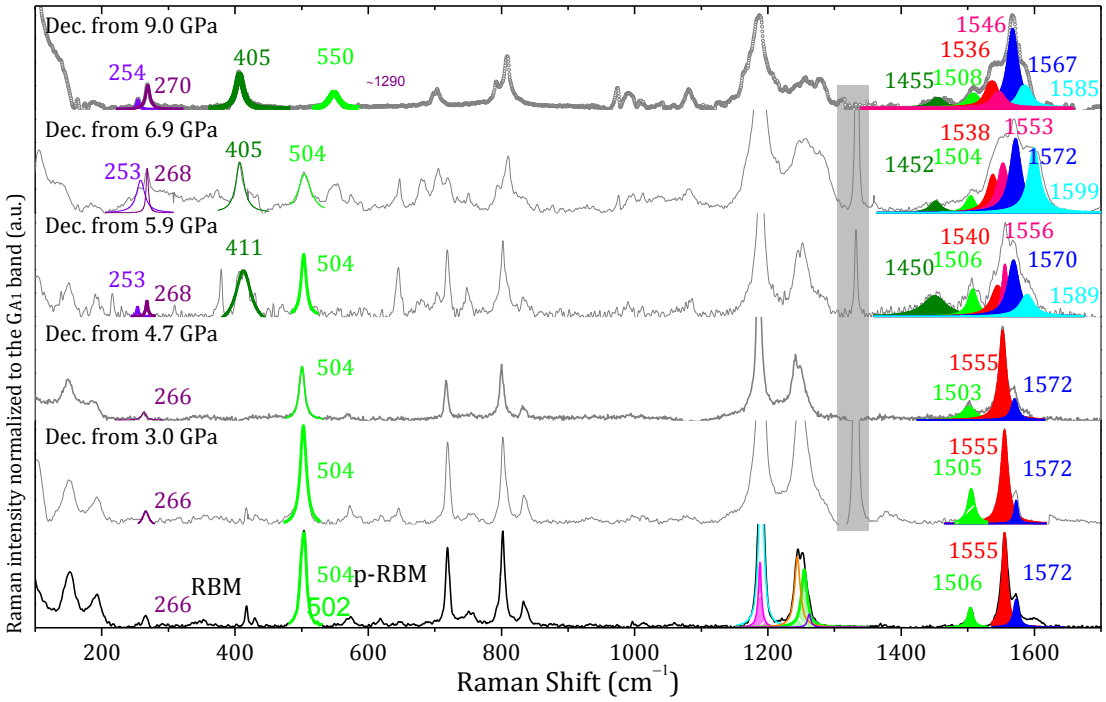

Figure 6. [5]CPP Experimental Raman spectra in the 100-1700 cm^{-1} region from bottom to top: the pristine sample (black line) and recovered samples after compressed up to the indicated pressure once pressure is released. The compression pressures are from bottom to top: 3.0, 4.7, 5.9, 6.9 and 9.0 GPa. Colored area corresponds to the Lorentzian fitting of the bands. Purple low frequency bands are assigned to the RBM, green low frequency bands to the p-RBM modes. In the high frequency regions the G_{io}, G_{A1} and G_{E2} are represented as green, red and dark blue areas, respectively.

As a general observation, due to the change of shape as expressed by the increasing flattening factor in Figure 3c, the vibrational spectrum becomes more complex as the pressure is increased. Strong bands split into subbands, as seen in both the experiments and the simulations. Given the characteristics of the experimental spectra, we follow each subband as a function of pressure and then compare these with the computed peaks. Given the large number of peaks in the computation with very small intensities, we selected the most intense bands in the computations. Figure 7 shows the experimental and computed Raman frequencies for both the HBP and PP models as the pressure is increased in the molecular phase. We compare these computed and observed frequency trends below.

At the low frequency ranges the Raman frequencies show relatively limited changes. In the higher frequency ranges the bands fan out beginning at about 4-5 GPa. Similar changes are seen in the simulations beginning at 3 – 5 GPa in the HBP model and ~11 GPa in the PP model. A particularly prominent feature of the PP simulation is the radical change of the frequencies of the molecular phase at around the 11 GPa pressure where polymer-1 becomes more stable and the molecular phase become metastable. The computed bands do not show a dramatic transition in a specific pressure range, but they do show a gradual splitting and fanning out as expected due to the lowering of the symmetry as the flattening factor is increasing. We will return to the issue of interpretation of the splitting vs. transition to the polymeric phases at the end.

The low frequency region includes vibrations in the 220-520 cm^{-1} and the 680-900 cm^{-1} ranges shown in Figure 7. Overall, there are modest shifts which will be analyzed below. For the lowest two (RBM) bands which is the radial breathing mode start to separate around 2-3 GPa and the frequency difference becomes larger under increasing pressure. For the rest of the bands we see also modest changes in the 400 to 520 cm^{-1} region. For the bands in the 780 to 830 cm^{-1} region we see a spreading of the bands starting at about 5-6 GPa. This band broadening and splitting effect is because the high pressure lowers the symmetry of the molecules.

In the middle region from 1150 to 1350 cm^{-1} there is a clear cut splitting of the two groups of bands. The intensity ratio of these two bands is closely related to the bond length alternation (BLA).[18] An initial increase of the frequency as a function of pressure is well reproduced by the computations. For the bands in the 1240 to 1350 cm^{-1} region we see a spreading of the bands starting at about 4-6 GPa.

Next we turn to the highest frequency region that provides most of the information on the changes of the BLA.[18] There are two main contributions ($G_{A1'}$and $G_{E2'}$), represented as red and blue profiles in Figure 6, at 1550 cm^{-1} and 1572 cm^{-1}, respectively. We have already reported and explained that the Raman shift of these bands are directly related with the structural BLA of the [n]CPP and with the quinonoid/aromatic ratio.[18, 28] The initial increase of the frequency as a function of pressure is well reproduced by the computations. Two main bands at 1550 and 1580 cm^{-1} start to split from ~2GPa, which is also observed in the RBM mode in low frequency region (200-300 cm^{-1}). Two new subbands emerge from the main bands and Raman frequencies continue to rise at different rates. These rates are presented as the slopes of pressure dependence of Raman frequencies in Table 3. The frequency increase effect of these BLA mode is correlated to the decrease of the bond length alternation in Figure 5a, indicating a direction of the structural transformation from aromatic to quinonoid.[29]

Table 3 contains the Raman frequencies rates defined as the slopes of Raman frequencies as a function of P for selected peaks. The general trend both in the calculations and the experiments is that most the Raman frequencies increase with increasing pressure within the investigated region with slopes ranging from -2 to 8 cm^{-1}/GPa with an overall average slope of about 3cm^{-1}/GPa. The two models predict different slope values but both tend to give larger slopes for the bands above 1150 cm^{-1} in general agreement with the experiments. Note that there is a large error associated with the slope values for both the simulation and the experiment for different reasons. In the experiment, the decomposition of the different peaks proceeds individually at each pressure, which does not sometimes provide a smooth shift of the peaks from pressure to pressure especially for the weaker peaks. In the simulation the optimization proceeds separately for each pressure

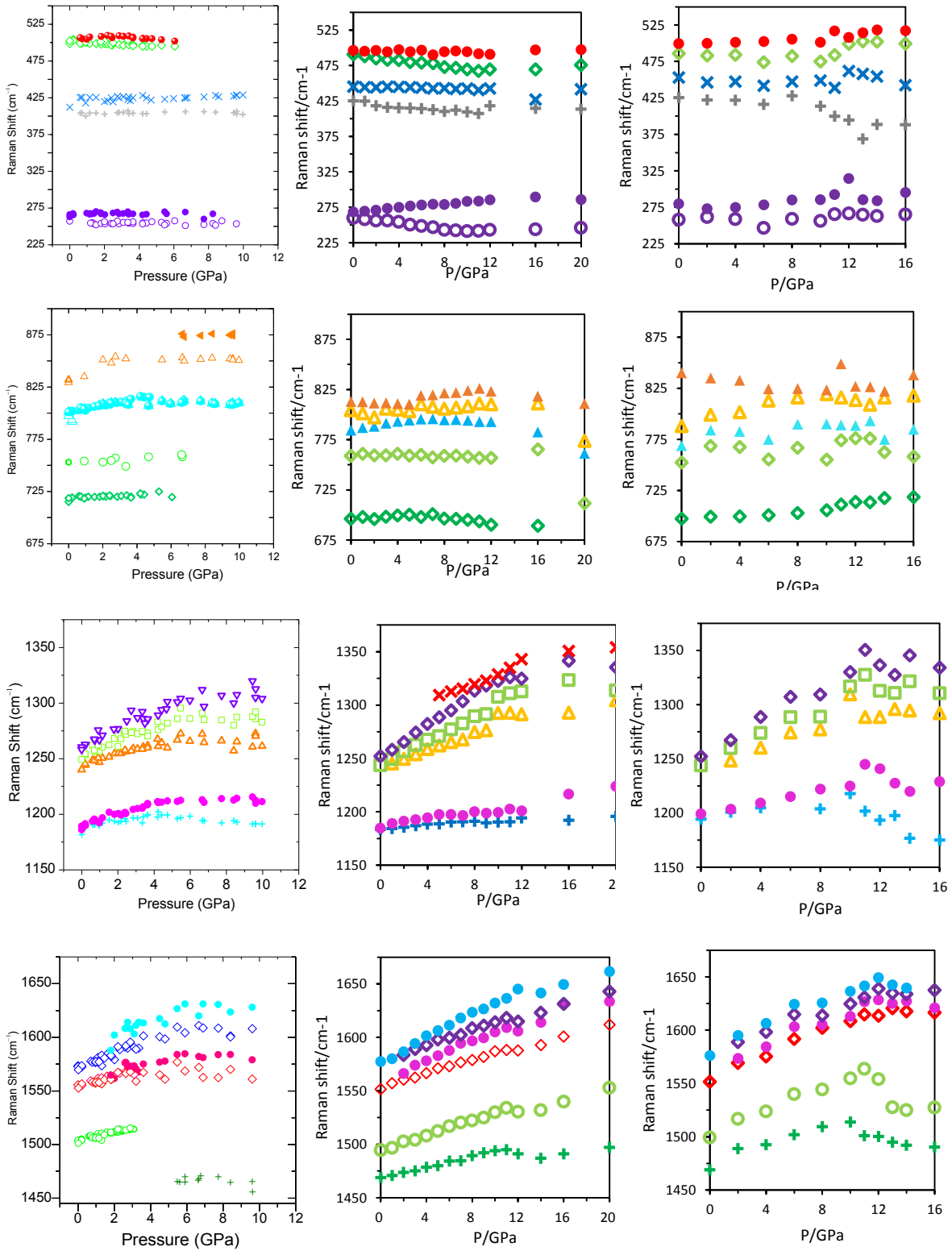

Figure 7. Experimental (left column) and computed (middle: HBP, right: PP model) Raman frequencies of [5]CPP measured and computed as a function of increasing pressure. Only the molecular phase simulation data are included.

causing some minor fluctuation in the computed parameters related to soft modes, such as torsions and flattening factors, as can be also seen e.g. Figures 3c and 5c.

Table 3. Slopes of pressure dependence of Raman frequencies for [5]CPP (in cm^{-1}/GPa).

Experimental frequency at P=0 (in cm^{-1})	Expt. slope at P=0[a]	Calc. slope at P=0 in HBP model[b]	Calc. slope at P=0 in PP model[b]
257	0.5	-1.3	-0.6
266	0.4	1.7	0.8
406	-1.1	-2.8	-0.1
420	0.6	-0.1	-0.8
502	-1.1	-2.1	-0.8
505	0.7	0.1	0.7
719	0.6	0.7	0.6
790	NA	2.2	3.8
802	2.9	0.6	3.5
832	3.2	0.0	3.5
1188	2.9	1.2	2.6
1190	5.1	2.3	2.7
1240	4.8	4.5	6.5
1244	6.3	6.1	7.4
1254	7.6	7.7	9.3
1504	3.5	3.4	6.5
1555	3.6	3.5	6.3
1555 split[c]	4.7	6.0	7.4
1572	6.9	4.6	7.8
1572 split[c]	~12.5[d]	6.3	6.5

[a]Slopes at P=0 are calculated between two points at P=0 and P=3.6 GPa.

[b]Slopes at P=0 are calculated between two points at P=0 and P=3 GPa.

[c]The second band with the same frequency label is split off as the pressure is increased, see Figure 6. This is the band with the higher frequency of the two.

[d]The experimental value has a large error because this band overlaps with the 1572 cm^{-1} band at pressures < 2 GPa.

While there are some non-systematic variations, as expected, we also see some trends in the slopes of pressure dependence of Raman frequencies. The frequencies above 1150 cm^{-1} tend to show larger slope values in agreement with the fact that they are connected to the BLA mode which changes very significantly as discussed in connection with Figure 3a. RBM modes as expected are less sensitive to the changes of pressure because the global change of the shape is gradual and distributed as opposed to the BLA mode that is changing the local force constants significantly.

The correlation of the computed and experimentally determined Raman shift rates as a function of pressure are shown in Figures 6 and S11. The agreement between computation and experiment is not perfect but the correlation is good indicating that the computational modeling is qualitatively correct. This is important because the initial slope of many of the bands changes

from a higher positive value to a lower value in the 2-6 GPa range in the modeling. We do not see a specific narrow pressure range where this transition occurs. The broadening and splitting of Raman bands occurs gradually in the computational modeling also. This can help to interpret the experimental data only because the experiment – computation correlation is reasonably good. Therefore, we conclude that the computations do not support the idea that there is a sudden structural transition occurring at around 5-6 GPa. An interpretation that emphasizes the gradual lowering of the symmetry as expressed by the change of the flattening factor and especially the BLA parameter explains the band splittings and the Raman shift rates in a quantitatively satisfactory fashion in both the HBP and PP model.

We turn to the issue of reversibility/irreversibility of the Raman spectra. The Raman spectra for four full up-down pressure cycles are given in Figures S4 – S7 with P_{max} = 3, 4.7, 5.9 and 6.9 GPa. The spectra are fully recoverable if the pressure cycling stops at a maximum pressure of approximately 5.9 GPa. In the experiment with cycling up to 7 GPa and back many key features of the spectra are suddenly lost and new features appear in the 400 to 800 cm^{-1} region. All peaks broaden upon pressure cycling when the top pressure exceeds 5.9 GPa. We do not know the precise onset of this broadening upon release, but it is present at the maximum pressure of 6.9 GPa.

From the modeling the following interpretation is suggested. As the pressure reaches the critical value when polymer-1 can be formed a process of polymerization begins. We have no information on the details of this process, and to what extent it proceeds throughout the sample. However, the formation of linked [5]CPP molecules above the critical pressure irreversibly generates products that have new Raman active bands. Their formation leads to an amorphous material with broadened Raman bands and we do not make an attempt to computationally predict their spectra.

This interpretation has limitations for the following reasons. The modeling uses simplified unit cells to begin with and the two models, HBP and PP treat the two types of intermolecular environments that are both present in the P=0 structure separately. Thus, while in the real material both environments are simultaneously present, this is not the case in the models. It is clear that the parallel packing (PP) environment produces the kinds of molecule to molecule overlap that breaks the conjugation in the [5]CPP molecules first as the pressure is increased in the simulation. It would be unrealistic to expect that this qualitative change would occur at pressures directly compatible with the experimentally observed pressures where such a bond breaking–bond making transformation also occurs as evidenced by the irreversibility of the Raman spectra. Second, the mechanism of the polymer formation is likely to occur in a non-uniform manner, given the deviations form hydrostatic conditions in the samples. For these reasons the computationally simulated critical pressure to polymer-1 occurs at a higher pressure than the limit of reversibility as observed by Raman spectroscopy.

Figure S13 shows the computed band gap as a function of pressure based on the optimized geometries along the k-space path (Γ- L- M- X-Γ), shown in Figure S12. The energy bands are quite narrow as expected for a molecular crystal although the bandwidths increase with increasing pressure. The dependency of the gap as function of pressure shows decreasing gaps with the increasing pressure which can be qualitatively understood by referring to the structure transformation from aromatic to quinonoid as indicated by the reduction of the BLA with increasing pressure. This trend should remain valid at other levels of DFT, even though it is well known that

PBE band gap values are generally underestimated. The bandgaps of polymer-1 and especially polymer-2 are relatively large at all pressures in the pressure range investigated due to the lack of conjugation along the polymer chains that is interrupted by the sp^3 hybridized carbon atoms linking the modified [5]CPP nanohoop units.

Conclusions

The pressure dependent Raman spectra of [5]CPP, the smallest diameter nanohoops synthesized so far, has been measured up to 10 GPa and computationally modeled for hydrostatic pressures up to 20 GPa. The structures have been simulated by the QE code. We have discovered two stable polymeric phases that arise in the simulation at two different critical pressures: polymer-1 and polymer-2 that appear at ~11 GPa and ~16 GPa, respectively. The critical pressures in the simulation are too high, but the formation of polymeric phases at high pressures provides a natural explanation for the irreversibility of the Raman spectra upon pressure release between 6 and 7 GPa. We characterize the geometrical changes of the nanohoops in the molecular phase upon pressure by monitoring their BLA, interring torsion and the flattening factors. The computed spectra show very good correlation with the experimental ones. The Raman bands show a general tendency of frequency increase, with some exceptions. These shifts are connected with of the changes of the geometrical parameters, especially the BLA. We find that the reduction of the BLA from an aromatic structure in the direction of a quinonoid structure is key to interpret the Raman data, while the torsions and flattening also play a secondary role. The gradual increase of the flattening reduces the symmetry of the nanohoops making more vibrational modes borrow Raman intensity from the lower number of high intensity bands at P=0 when the symmetry is highest. The trends in the bandgap, a strong reduction of the gap with increasing pressures, is in good correlation with data on [n]CPPs where the correlation with BLA was established. Here we attribute the reduction of the gap with increasing pressure to the decrease in BLA as P is increased. In conclusion, this work demonstrates that in combination with modern DFT solid state calculations, Raman spectroscopy can help provide atomistic level description of complex organic molecules and their reactivity under high pressures.

Supporting information:

Calibration data for pressure and volume, pressure dependent unit cell parameters, spectra at selected pressures and band structures, chemical structures of polymer-2 are given in the SI section.

Authorship information:

Lili Qiu and Miklos Kertesz are responsible for the computational modeling; Miriam Peña-Alvarez, Mercedes Taravillo, Juan Casado, Valentín G. Baonza, Juan T. López Navarrete, P. Mayorga Burrezo are responsible for the high pressure Raman experiments; Paul J. Evans, Evan R. Darzi and Ramesh Jasti synthesized the samples; the manuscript was written by Lili Qiu and Miklos Kertesz with significant contributions from Miriam Peña-Alvarez and Juan Casado.

Acknowledgements:

We thank the U. S. National Science Foundation for its support of this research at Georgetown University (grant number CHE-1006702). Financial support from MINECO, Government of Spain is acknowledged (project reference FEDER CTQ CTQ2015-69391-P). This work has been also

supported by MINECO through the projects CSD2007-00045, CTQ2012-38599-C02-02 and CTQ2013-48252-P. MPA is grateful to the Spanish Ministerio de Educación, Cultura y Deporte for an FPU grant. The work at the University of Oregon was funded by the National Science Foundation (grant number CHE-1255219).

References

[1] M. R. Golder and R. Jasti, *Acc. Chem. Res*. 2015, **48**, 557-566.

[2] P. Li, T. J. Sisto, E. R. Darzi and R. Jasti, *Org. Lett.* 2014, **16**, 182−185

[3] R. Jasti, J. Bhattacharjee, J. B. Neaton and C. R. Bertozzi, *J. Am. Chem. Soc.* 2008, **130**, 17646–17647.

[4] J. Xia and R. Jasti, *Angew. Chem. Int. Ed.* 2012, **51**, 2474–2476.

[5] (a) H. Omachi, T. Nakayama, E. Takahashi, Y. Segawa and K. Itami, *Nat. Chem.* 2013, **5**, 572–576. (b) E. R. Darzi, B. W. White, L. K. Loventhal, L. N. Zakharov and R. Jasti, J. Am. Chem. Soc. 2017, **139**, 3106-3114.

[6] P. J. Evans, E. R. Darzi and R. Jasti, *Nat. Chem*. 2014, **6**, 404-408.

[7] Y. Segawa, H. Omachi and K. Itami, *Org. Lett*. 2010, **12**, 2262–65.

[8] M. Peña-Alvarez, M. C. R. Delgado, M. Taravillo, V. G. Baonza, J. T. L Navarrete, P. Evans, R. Jasti, S. Yamago, M. Kertesz, and J. Casado, *Chem. Sci.* 2016, **7**, 3494-3499.

[9] J. Tang, L.-C. Qin, T. Sasaki, M. Yudasaka, A. Matsushita and S. Iijima, S. *Phys. Rev. Lett.* 2000, **85**, 1887−1889.

[10] A. Merlen, N. Bendiab, P. Toulemonde, A. Aouizerat, A. San Miguel, J. L. Sauvajol, G. Montagnac, H. Cardon, and P. Petit, *Phys. Rev. B* 2005, **72**, 035409.

[11] M. Yao, Z. Wang, B. Liu, Y. Zou, S. Yu, W. Lin, Y. Hou, S. Pan, M. Jin, B. Zou, T. Cui, G. Zou, and B. Sundqvist, *Phys. Rev. B* 2008, **78**, 205411.

[12] M. H. F. Sluiter, V. Kumar, and Y. Kawazoe, *Phys. Rev. B* 2002, **65**, 161402.

[13] S. M. Sharma, S. Karmakar, S. K. Sikka, P. V. Teredesai, A. K. Sood, A. Govindaraj and C. N. R. Rao, *Phys. Rev. B* 2001, **63**, 205417.

[14] S. Rols, I. N. Gontcharenko, R. Almairac, J. L. Sauvajol and I. Mirebeau, I. *Phys. Rev. B* 2001, **64**, 153401.

[15] A. Jorio, M. A. Pimenta, A.G.S. Filho, R. Saito, R. G. Dresslhaus, and M.S. Dresselhaus, *New J. Phys*. 2003, **5**, 139.1-139.17.

[16] A. L. Aguiar, R. B. Capaz, A. G. S. Filho and A. San-Miguel, *J. Phys. Chem. C* 2012, **116**, 22637-22645.

[17] A. N. Imtani and V. K. Jindal, *Comput. Mater. Sci.* **2009**, *46*, 297−302.

[18] M. Peña-Alvarez, L. Qiu, L. M. Taravillo, V.G. Baonza, M.C.R. Delgado, S. Yamago, R. Jasti, J. T. L Navarrete, J. Casado, and M. Kertesz, *Phys. Chem. Chem. Phys*. 2016, **18**, 11683-11692.

[19] (a) J.-L. Bredas, R. R. Chance and R. Silbey, *Phys. Rev. B* 1982, **26**, 5843-5854. (b) T. A. Skotheim, Ed.; Dekker. *Handbook of Conducting Polymers*; New York, 1986; Vols. 1 and 2. (c) J.-L. Bredas and R. R. Chance, Eds.; *Conjugated Polymeric Materials*; Kluwer Academic: Dordrecht, 1990. (d) Y. S. Lee, M. Kertesz and R. L. Elsenbaumer, *Chem. Mater*. 1990, **2**, 526-530.

[20] V. G. Baonza, M. Taravillo, A. Arencibia, M. Cáceres and J. Núñez, *J. Raman Spectrosc*. 2003, **34**, 264-270.

[21] E. del Corro, M. Taravillo, J. González and V. G. Baonza, *Carbon*, 2011, **49**, 973-979.

[22] P. Giannozzi, S. Baroni, N. Bonini, M. Calandra, R. Car, C. Cavazzoni, D. Ceresoli, G. L. Chiarotti,

M. Cococcioni, I. Dabo, A. Dal Corso, S. Fabris, G. Fratesi, S. de Gironcoli, R. Gebauer, U. Gerstmann, C. Gougoussis, A. Kokalj, M. Lazzeri, L. Martin-Samos, N. Marzari, F. Mauri, R. Mazzarello, S. Paolini, A. Pasquarello, L. Paulatto, C. Sbraccia, S. Scandolo, G. Sclauzero, A. P. Seitsonen, A. Smogunov, P. Umari, and R. M. Wentzcovitch, *J. Phys. Condens. Matter*, 2009, **21**, 395502.

[23] We used the pseudopotentials C.pbe-n-rrjkus_psl.UPF and H.pbe-rrkjus_psl.UPF from the Quantum ESPRESSO pseudopotential data base:
http://www.quantum-espresso.org/pseudopotentials.

[24] A. M. Rappe, K. M. Rabe, E. Kaxiras, and J. D. Joannopoulos, *Phys. Rev. B*, 1991, **44**, 13175.

[25] Gaussian 09, Revision A.02, M. J. Frisch, G. W. Trucks, H. B. Schlegel, G. E. Scuseria, M. A. Robb, J. R. Cheeseman, G. Scalmani, V. Barone, B. Mennucci, G. A. Petersson, H. Nakatsuji, M. Caricato, X. Li, H. P. Hratchian, A. F. Izmaylov, J. Bloino, G. Zheng, J. L. Sonnenberg, M. Hada, M. Ehara, K. Toyota, R. Fukuda, J. Hasegawa, M. Ishida, T. Nakajima, Y. Honda, O. Kitao, H. Nakai, T. Vreven, J. A. Montgomery, Jr., J. E. Peralta, F. Ogliaro, M. Bearpark, J. J. Heyd, E. Brothers, K. N. Kudin, V. N. Staroverov, R. Kobayashi, J. Normand, K. Raghavachari, A. Rendell, J. C. Burant, S. S. Iyengar, J. Tomasi, M. Cossi, N. Rega, J. M. Millam, M. Klene, J. E. Knox, J. B. Cross, V. Bakken, C. Adamo, J. Jaramillo, R. Gomperts, R. E. Stratmann, O. Yazyev, A. J. Austin, R. Cammi, C. Pomelli, J. W. Ochterski, R. L. Martin, K. Morokuma, V. G. Zakrzewski, G. A. Voth, P. Salvador, J. J. Dannenberg, S. Dapprich, A. D. Daniels, O. Farkas, J. B. Foresman, J. V. Ortiz, J. Cioslowski, and D. J. Fox, Gaussian, Inc., Wallingford CT, 2009.

[26] B. Chen, R. Hoffmann, N. W. Ashcroft, J. V. Badding, E. Xu, and V. H. Crespi, *J. Am. Chem. Soc*. **2015**, *137*, 14373-14386.

[27] T. Fitzgibbons, M. Guthrie, E.-S. Xu, V. H. Crespi, S. K. Davidowski, G. D. Cody, N. Alem, and J. V. Badding, *Nat. Mater*. **2015**, *14*, 43-47.

[28] M. Peña-Alvarez, P. M. Burrezo, M. Kertesz, T. Iwamoto, S. Yamago, J. Xia, R. Jasti, L. J. T. Navarrete, M. Taravillo, V. G. Baonza, and J. Casado, *Angew. Chem. Int. Ed*. 2014, **53**, 7033-7037.

[29] L. Cuff, C. X. Cui, M. Kertesz, *J. Am. Chem. Soc*. 1994, **116**, 9269-9274.